73nd International Astronautical Congress (IAC), Paris,France, 18-22 September 2022.

IAC-22,C1,IPB,5,x71401

Exploiting coherent patterns for the analysis of qualitative motion and the design of bounded orbits around small bodies

Nicoló Bernardini[1], **Gianmario Merisio**[2], **Matteo Losacco**[3], **Sebastiano Raffa**[4], **Roberto Armellin**[5], **Nicola Baresi**[6], **Stephanie Lizy-Destrez**[7], **Francesco Topputo**[8], and **Elisabet Canalias**[9]

Missions around small bodies present many challenges from their design to the operations, due to the highly non-linear and uncertain dynamics, the limited Δv budget and constraints coming from orbit determination and mission design. Within this context, mathematical tools to enhance the understanding of the dynamics behavior can be proven useful to support the mission design process. Chaos indicators are adopted to reveal patterns of time-dependent dynamical systems and to enable the identification of practical stability regions, which are then exploited to design bounded orbits in the proximity of small bodies. The methodology is applied to study the MMX and Hera missions. In the MMX context, the final goal is to obtain bounded orbits useful for the global surface mapping and gravity potential determination of Phobos. On the other hand, concerning the Hera mission, a qualitative analysis of the natural motion about the Didymos binary asteroid system is carried out to compute bounded orbits convenient for the global characterization of the two asteroids and to investigate potential landing trajectories. Sensitivity analyses via Monte Carlo simulations are performed to prove the robustness of the different bounded orbits.

1 Introduction

Interest towards asteroids and small planetary bodies drastically increased in the last decade thanks to the central role they play in the understanding of the formation our solar system [1], for the opportunity they give for gathering resources through mining [2] and also for the potential hazard they present in the context of planetary defence [3].

However, designing and operating missions around small bodies are challenging tasks due to the limited ΔV budget, highly perturbed and uncertain dynamics, and constraints coming from orbit determination and communication with the ground station. A primary objective for a good outcome of these missions is to design operational orbits that meet mission requirements, require low fuel consumption for their maintenance and transfers, and that are robust to uncertain parameters and unmodeled dynamics. Within this context, mathematical tools to improve the understanding of the behavior of the dynamics can shown to be useful to support the mission design process.

In this study, the more general approaches for the characterization of the dynamical system is investigated. Based on the experience from the fluid dynamics field, it is possible to exploit the intrinsic information embedded within coherent patterns of dynamical systems to better understand the underlying structure that is responsible for the creation of such features [4–6]. These features and different behaviours in the dynamics can be identified by Lagrangian coherent structures (LCS). LCSs enable to distinguish regions of qualitatively different dynamics in the state space throughout time [4]. A lot of research has been performed on LCSs and the way to compute them. Different indicators, like finite-time Lyapunov exponents, trajectory length indicators, probabilistic transfer operator and many others [7] have been found useful to highlight coherent structures in the phase space of non-linear dynamical systems and in [4, 8] a variational theory approach to LCSs presents the sufficient and necessary conditions for the existence of LCSs and their numerical implementation for two dimensional dynamical models and expanded to three dimensional system in [9, 10].

These different indicators have already been used in the field of astrodynamics for different applications in perturbed two body problems [11] and for N-body problems [12–14]. Some examples of those, focused on the ballistic capture topic, are found in [10, 15, 16]. In [17] preliminary studies showed that chaoticity maps, obtained with fast Lyapunov indicators (FLI), can be used to locate favorable regions in the phase space in which the orbits for the Martian Moons eXploration (MMX) mission could be placed.

[1]PhD Candidate, Surrey Space Centre, University of Surrey, GU2 7XH, Guildford, United Kingdom; n.bernardini@surrey.ac.uk

[2]PhD Candidate, Department of Aerospace Science and Technology, Politecnico di Milano, Via La Masa 34, 20156, Milano, Italy; gianmario.merisio@polimi.it

[3]Department of Aerospace Vehicles Design and Control, ISAE-SUPAERO, 10 avenue Édouard-Belin, 31400, Toulouse, France; Matteo.LOSACCO@isae-supaero.fr

[4]MSc, Department of Aerospace Science and Technology, Politecnico di Milano, Via La Masa 34, 20156, Milano, Italy; sebastiano.raffa@mail.polimi.it

[5]Full Professor, Te Pūnaha Ātea - Auckland Space Institute, University of Auckland, Auckland, New Zealand; roberto.armellin@auckland.ac.nz

[6]Lecturer, Surrey Space Centre, University of Surrey, GU2 7XH, Guildford, United Kingdom; n.baresi@surrey.ac.uk

[7]Associate Professor, Department of Aerospace Vehicles Design and Control, ISAE-SUPAERO, 10 avenue Édouard-Belin, 31400, Toulouse, France; Stephanie.LIZY-DESTREZ@isae-supaero.fr

[8]Full Professor, Department of Aerospace Science and Technology, Politecnico di Milano, Via La Masa 34, 20156, Milano, Italy; francesco.topputo@polimi.it

[9]CNES, 18 Av. Edouard Belin, 31400 Toulouse, France; elisabet.canalias@cnes.fr

This work generalizes the concept of invariant manifolds theory to non-autonomous dynamical systems and performs a qualitative analysis of the dynamics around small bodies in order to highlight practical stability regions. The methodology is applied to the case studies of MMX and Hera missions.
The developed technique is used to obtain bounded orbits in the case of motion about Martian moons (within the context of MMX mission) and binary asteroids (in the framework of Hera mission). Regarding MMX mission, a qualitative analysis of the natural motion about the martian moons, in particular Phobos, is performed. The goal is to obtain bounded orbits useful for the global surface mapping and gravity potential determination of Phobos [18]. On the other hand, in relation to Hera mission, a qualitative analysis of the natural motion about the Didymos binary asteroid system is carried out to compute bounded orbits useful for the global characterization of the asteroids belonging to the system and to investigate potential landing trajectories. To conclude, sensitivity analyses are performed on the different trajectories for both cases with Montecarlo simulations in order to assess the robustness to injections errors of the different initial conditions.

2 Chaos indicators

In autonomous dynamical systems invariant manifold theory is very useful in determining the qualitative properties of groups of trajectories. They act as separatrix of the phase space for problems with less than two degrees of freedom and the trajectories show different behavior depending on the side of the manifold in which they are located. The big advantage of invariant manifolds is that, being the system autonomous, they remain invariant with respect to time, in accordance with the independence of the dynamical system from the independent variable. The behavior of an autonomous dynamical system, with respect to its initial condition, can be completely studied via fixed points. However, these properties are lost in the case of non-linear non-autonomous dynamical systems, linked to complex dynamical phenomena.
A mathematical tool suited to study complex non-linear non-autonomous dynamical systems is represented by LCSs [4, 13, 19, 20]. The word Lagrangian highlights the evolution of such structures in the state space throughout time, as opposed to the Eulerian specification of the flow. LCSs represent a robust skeleton of special material surfaces which distinguish regions of qualitatively different dynamics [6]. For this reason, LCSs can be considered as a generalization of invariant manifolds in non-autonomous systems with arbitrary time dependence. They are time-evolving structures in the phase space of a generic dynamical system which form the skeleton of observed tracer patterns. The definition of a LCS is based on two key properties [4]:

- a LCS should be a material surface, since it must have sufficiently high dimension to have visible impact and act as a transport barrier, and it must move with the flow to act as an observable core of evolving Lagrangian patterns;
- a LCS should exhibit locally the strongest attraction, repulsion or shearing in the flow, which is essential to distinguish a LCS from all nearby material surfaces.

In particular, repelling LCSs are the core structures, generating stretching. On the other hand, attracting LCSs act as centerpieces of folding. Finally, shear LCSs delineate swirling and jet-type patterns. Thus, from their physical interpretation, LCSs result of very interest for the study of the dynamics. They separate different dynamics of the flow in space and time, acting as the most important barriers for material flux across them. LCSs can be classified following the same logic used when analyzing invariant manifolds:

- hyperbolic LCSs are structures characterized by the strongest attraction/repulsion;
- elliptic LCSs are closed material surfaces;
- parabolic LCSs are structures characterized by the strongest shearing.

When considering autonomous dynamical systems, examples of LCSs are stable and unstable manifolds of fixed points and periodic orbits. The big advantage of LCSs is that they still remain applicable to more complex flows with arbitrary time dependence or only defined over a finite time interval (computed or measured). While in autonomous systems LCSs correspond to invariant manifolds, in time-dependent ones LCSs evolve with the flow while continuing to bound distinct regions of behavior [21].
In order to detect LCSs in the phase space different indicators and methodologies are present in literature [7]. For this research the main indicators investigated are the Lagrangian Descriptors (LD).

2.1 Lagrangian Descriptor

LDs are a heuristic technique for revealing the underlying template of geometrical structures that determine transport in phase space for a generic dynamical system [22]. In essence, LDs are based on the integration of a bounded, positive property of the trajectory for a finite time [22]. The first definition of LD relied on the computation of the arc length of particle trajectories as they evolve forward and backward in time [23]. Later, the method was extended to include other positive quantities. The methodology found several applications in different scientific areas, such as ocean currents, atmospheric sciences, and chemistry [22, 23].
Let's consider a general time-dependent vector field on $\mathbb{R}^n$

$$\frac{\mathrm{d}\mathbf{x}(t)}{\mathrm{d}t} = \mathbf{v}(\mathbf{x}, t), \text{ with } \mathbf{x} \in \mathbb{R}^n, \text{ and } t \in \mathbb{R}. \qquad (1)$$

Assuming the velocity field C^r ($r \geq 1$) in $\mathbf{x}$ and continuous in t, a unique solution allowing for linearization exists. M_1 is the

Tab. 1: Different LDs with integrand and used norm [22].

LD	Integrand	Norm
M_1	magnitude of velocity	L^1
M_2	magnitude of acceleration	L^1
M_3	magnitude of acceleration or velocity	$L^{\frac{1}{2}}$ or L^2
M_4	magnitude of time derivative of acceleration	L^1
M_5	positive quantity related to curvature	L^1

Euclidean arc length of the curve in the phase space defined by propagating an initial state $\mathbf{x}(t^*) = \mathbf{x}^*$ through Eq. (1). The initial time is t^* and the integration time interval is $[t^*-\tau, t^*+\tau]$. M_1 is computed as follow [22]:

$$M_1(\mathbf{x}^*, t^*, \tau) = \int_{t^*-\tau}^{t^*+\tau} \sqrt{\sum_{i=1}^{n} \left(\frac{\mathrm{d}x_i(t)}{\mathrm{d}t}\right)^2}\mathrm{d}t = \\ = \int_{t^*-\tau}^{t^*+\tau} ||\mathbf{v}(\mathbf{x}, t)||\mathrm{d}t. \tag{2}$$

Trajectories propagated from close initial conditions that remain close as they evolve in time are expected to have similar M_1 [22]. Differently, boundaries between regions comprising trajectories with qualitatively different behavior are expected to exhibit an abrupt change in the derivative of M_1 along the direction perpendicular to these boundaries [22]. Results depend on the integration time span chosen, in particular on the selected $(\mathbf{x}^*, t^*)$ and τ. In addition to the M_1 indicator, there exist other positive intrinsic physical or geometrical properties of trajectories that can be integrated to successfully identify the geometrical structures of underlying template characteristic of the dynamical system. The general formulation is written as follows:

$$\begin{cases} M(\mathbf{x}^*, t^*, \tau) = \displaystyle\int_{t^*-\tau}^{t^*+\tau} |\mathcal{F}(\mathbf{x}(t))|^\gamma dt & \text{for } \gamma \leq 1 \\ M(\mathbf{x}^*, t^*, \tau) = \Big(\displaystyle\int_{t^*-\tau}^{t^*+\tau} |\mathcal{F}(\mathbf{x}(t))|^\gamma dt\Big)^{\frac{1}{\gamma}} & \text{for } \gamma > 1 \end{cases} \tag{3}$$

where γ defines the L^γ norm of the integrand. Several types LDs are listed in Table 1. The definition of any function M_i can be broken in a natural way into forward (M_i^f) and backward (M_i^b) integration. The forward integration should highlight stable manifolds of the dynamical system, while the backward propagation recovers unstable ones [21, 24]. The great advantage of LD is that to obtain the indicator is sufficient to include the integrand of Equation 3 into the dynamics; Algorithm 1 presents the procedure to obtain the LD scalar field.

$$\begin{cases} \dot{\mathbf{x}}(t) = \mathbf{f}(\mathbf{x}(t), t) \\ \dot{M} = |\mathcal{F}(\mathbf{x}(t))|^\gamma \mathbf{x}(t_0) = \mathbf{x}_0 \\ M(t_0) = 0 \ . \end{cases} \tag{4}$$

Procedure INITIALIZATION
  Define the grid of initial conditions G_0;
  Define the time initial time and the time interval $[t_0, \tau]$;
Procedure LD SCALAR FIELD
  for $\forall \mathbf{x}_0 \in G_0$
    Integrate forward, from t_0 to $t_0 + \tau$ the dynamics in Eq. 4 and obtain the final value of M, M_f^τ ;
    Integrate backward, from t_0 to $t_0 - \tau$ the dynamics in Eq. 4 and obtain the final value of M, M_b^τ;
    Compute $M(\boldsymbol{x}_0, t_0, \tau) = M_f^\tau - M_b^\tau$;
  end
  Plot $M(\boldsymbol{x}_0, t_0, \tau)$ $\forall \mathbf{x}_0 \in G_0$;
Result: LD scalar field.

Algorithm 1: LD computation.

The procedure just presented enables to compute the LD scalar field and it was show in how it used to detect the evolution of LCS and how it highlights both stable and unstable manifolds [22]. Since the focus of this study is not the identification of stable and unstable manifolds, but the main goal is study the evolution of the dynamics forward in time and the detection of bounded motion the results that are presented in the following sections utilize only the LD computed using the forward propagation (M_f^τ) while M_b^* is not computed.
Similar to other indicators, like the FTLE [7], the Lagragian Descriptors are heuristic indicators and do not present necessary and sufficient conditions for the existence of LCSs like the variational theory for LCSs [4] and the abrupt changes of the LDs might fail in identifying the LCs in certain situations. On the other hand, the implementation of LD indicators is simpler than the application of variational theory and it can be easily generalized to n-dimensional dynamics. In addition to that, the computation of LDs requires a very small computational effort since it is sufficient to integrate one additional term to the existing dynamics, enabling to obtain the desired map of the phase space in relatively short amount of time with a high grid resolution. In general, the LD indicators will be shown to be sufficiently accurate in capturing the main features of the phase space and in highlighting the practical stability regions which represent the main goal of this research.

3 Application to the MMX mission

3.1 Dynamics around Phobos

This section contains the equation of motion used to describe the dynamics in the proximity of Phobos that will be used later on in the study.

3.2 Equations of motion around Phobos

3.2.1 Eccentric Hill problem

To describe the motion around Phobos the dynamics is expressed in a rotating reference frame centred around the Martian Moon. The $\hat{\mathbf{x}}$ axis is always aligned with the Mars and Phobos direction and pointed from Mars to Phobos; the $\hat{\mathbf{z}}$ is parallel with the angular momentum of the orbit of Phobos around Mars while the $\hat{\mathbf{y}}$ completes the orthogonal triad [25] as shown in Figure 1.

For this study the Phobos barycenter is considered to be in an Keplerian eccentric orbit around Mars. The gravity of Phobos is modelled as a tri-axial ellipsoid and it is known that the martian satellite is in a tidal-locked configuration [25], meaning that the satellite completes a revolution around its main axis of inertia ($\hat{\mathbf{z}}$) in the same time it performs an orbital period around Mars. Thanks to the small ratio between the mass of the Martian moon and Mars and the close distance between the spacecraft and Phobos, the dynamics can be approximated by the elliptic Hill problem with the non-spherical gravity of Phobos as disturbance [25, 26] . The equations of motion are written as:

$$\dot{\mathbf{X}} = \begin{cases} v_x \\ v_y \\ v_z \\ 2v_y + \frac{3}{\gamma}x + g_x \\ -2v_x + g_y \\ -z + g_z \end{cases} \tag{5}$$

where the dot represent the differentiation with respect to the true anomaly of Phobos; $\mathbf{X} = [x, y, z, \dot{x}, \dot{y}, \dot{z}]$ is the spacecraft state in pulsating normalized coordinates; $\gamma = 1 + e_p \cos(\nu)$ and $\mathbf{g} = [g_x, g_y, g_z]$ is the acceleration given by the Martian Moon. The main physical parameters are listed in Table 2.

The gravitational acceleration given by Phobos can be computed as follow:

$$\mathbf{g} = kR_z[\Gamma]\mathbf{G} \tag{6}$$

where $k = p_p^2 \epsilon^{-1} \mu_M^{-1} \gamma^{-3}$, being $p_p = a_p(1 - e_p)$ the semi-latus rectum of Phobos's orbit and $\epsilon = \left(\frac{\mu_p}{\mu_M}\right)^{1/3}$; $R_z[\Gamma]$ represents a rotation matrix about the $\hat{\mathbf{z}}$ axis:

$$R_z[\Gamma] = \begin{bmatrix} \cos(\Gamma) & \sin(\Gamma) & 0 \\ -\sin(\Gamma) & \cos(\Gamma) & 0 \\ 0 & 0 & 1 \end{bmatrix} \tag{7}$$

where $\Gamma = \nu - M$ is the kinematic libration angle given by the difference between Phobos true and mean anomaly.

The vector $\mathbf{G} = [G_x, G_y, G_z]$ represents the gravity acceleration given by an ellipsoidally-shaped body [25]. The components in the principal axis frame of the Phobos are given by:

$$G_x = -\frac{3}{2}\mu_p X \int_0^\infty \left(\frac{1}{\overline{\alpha}^2 + \Lambda + l}\right) \frac{dl}{\Delta(l + \Lambda)} \tag{8a}$$

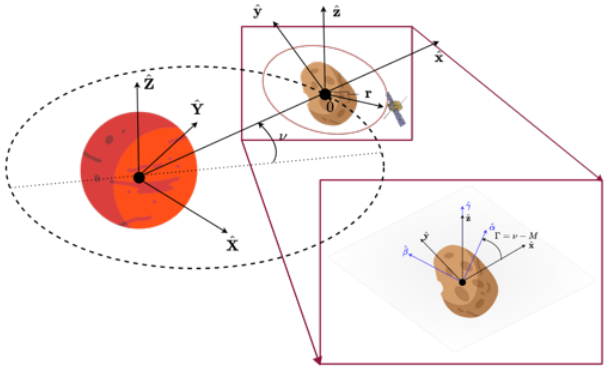

Fig. 1: Schematic representation of the dynamics around Phobos. In the red rectangle the libration of Phobos is highlighted

$$G_y = -\frac{3}{2}\mu_p Y \int_0^\infty \left(\frac{1}{\overline{\beta}^2 + \Lambda + l}\right) \frac{dl}{\Delta(l + \Lambda)} \tag{8b}$$

$$G_z = -\frac{3}{2}\mu_p Z \int_0^\infty \left(\frac{1}{\overline{\gamma}^2 + \Lambda + l}\right) \frac{dl}{\Delta(l + \Lambda)} \tag{8c}$$

where $\mathbf{R} = [X, Y, Z] = \epsilon p_p \gamma^{-1} R_z[-\Gamma][x, y, z]^T$ is the dimensional position of the spacecraft in the principal-axis frame of Phobos, $\overline{\alpha}, \overline{\beta}, \overline{\gamma}$ are the largest, intermediate and smallest semi-major axes of Phobos. The value $\Delta(l + \Lambda)$ is computed as:

$$\Delta(l + \Lambda) = \sqrt{(\overline{\alpha}^2 + \Lambda + l)(\overline{\beta}^2 + \Lambda + l)(\overline{\gamma}^2 + \Lambda + l)} \tag{9}$$

and Λ is the positive root of the following polynomial:

$$\frac{X^2}{\overline{\alpha} + \Lambda} + \frac{Y^2}{\overline{\beta}^2 + \Lambda} + \frac{Z^2}{\overline{\gamma}^2 + \Lambda} - 1 = 0 \ . \tag{10}$$

The three elliptic integrals in Equation 8a - 8b - 8c are computed numerically following Ref. [27].

Tab. 2: Physical properties

Symbol	Quantity	Value	Units
$\overline{\alpha}$	Largest semi-major axis	13.03	km
$\overline{\beta}$	Intermediate semi-major axis	11.40	km
$\overline{\gamma}$	Smallest semi-major axis	9.14	km
σ_P	Density	1.860	g/cm^3
M_P	Mass	1.058×10^{16}	kg
μ_P	Phobos Gravitational Parameter	7.060×10^{-4}	km^3/s^2
μ_M	Mars Gravitational Parameter	4.283×10^4	km^3/s^2
a_P	Phobos' semi-major axis	9377	km
P_P	Phobos rotational Period	7.66	hr
ω_P	Phobos spin Rate	2.279×10^{-4}	rad/s
e_P	Phobos orbit eccentricity	0.0151	-
LU	Unit length	23.92	km
TU	Time length	4387.63	s

3.2.2 *Orbit elements around Phobos*

It is possible to rewrite the dynamics previously presented by deriving a set of orbit elements. Ankersen and Yamanaka solved the Tschauner-Hempel equations analytically [28] while providing the expression of six integral of motions $K_1, K_2, K_3, K_4, K_5, K_6$. This allows to rewrite the state as:

$$\mathbf{X} = \begin{cases} x = K_2\gamma\sin(\nu) + K_3\gamma\cos(\nu) + \\ \quad + K_4\left(2 - 3eJ\gamma\sin(\nu)\right) \\ y = K_1 + K_2(1+\gamma)\cos(\nu) + \\ \quad - K_3(1+\gamma)\sin(\nu) - 3K_4J\gamma^2 \\ z = K_5\sin(\nu) + K_6\cos(\nu) \\ \dot{x} = K_2 s^* + K_3 c^* - 3eK_4\left(\frac{\sin(\nu)}{\gamma} + J^*\right) \\ \dot{y} = -2K_2\gamma\sin(\nu) - K_3(2\gamma\cos(\nu) - e) + \\ \quad - 3K_4(1 - 2eJ\gamma\sin(\nu)) \\ \dot{z} = K_5\cos(\nu) - K_6\sin(\nu) \end{cases} \tag{11}$$

where $s^* = \cos(\nu) + e\cos(2\nu)$, $c^* = \sin(\nu) + 2\sin(2\nu)$ and $J = \int_{\nu_0}^{\nu} 1/\gamma(\tau)^2 d\tau$. From the formulation in [29], it is possible to rewrite the six integrals of motion gaining a geometrical understanding of the Tschauner-Hempel equations:

$$A_x = K_3, \tag{12a}$$
$$A_y = K_2 - 3eJK_4, \tag{12b}$$
$$\delta_x = 2K_4, \tag{12c}$$
$$\delta_y = K_1 - 3JK_4, \tag{12d}$$
$$A = \sqrt{A_x^2 + A_y^2}, \tag{12e}$$
$$\alpha = \arctan\left(\frac{-A_y}{A_x}\right), \tag{12f}$$
$$B = \sqrt{K_5^2 + K_6^2}, \tag{12g}$$
$$\beta = \arctan\left(\frac{K_6}{K_5}\right). \tag{12h}$$

The position of the spacecraft can be rewritten as [30]:

$$\begin{cases} x(\nu) = \gamma A\cos(\nu + \alpha) + \delta_x \\ y(\nu) = -(1+\gamma)A\sin(\nu + \alpha) + \delta_y \\ z(\nu) = B\sin(\nu + \beta). \end{cases} \tag{13}$$

By observing Equation 13 it is clear that the spacecraft remains in the proximity of Phobos only if A, δ_x and δ_y remain bounded. It is guaranteed when $K_4 = 0$ since A_y and δ_y stay constant even if the integral term J is present [30]. The variable A represents the semi-major and semi-minor axis of the ellipse while the position of the center of the ellipse is described by δ_x and δ_y; it could be possible to associate the variable A to the semi-major axis of Keplerian orbits when the satellite is relatively far from Phobos, but when the trajectories of interest get closer to the Martian moon it is not possible to consider A alone since the three variables, A, δ_x, δ_y, together describe the shape of the trajectory on the plane. The variables α and β represent the fast changing variable of the system while K_5 and K_6 describe the out-of-plane motion.
The geometric interpretation of this new set of parameters is shown in Figure 2a - 2b. As for the out-of-plane motion, it is decoupled from the planar one like in the Tschauner-Hempel equations and it behaves like an harmonic oscillator.

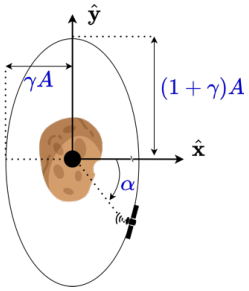

(a) Schematic representation of the physical meaning of A and α

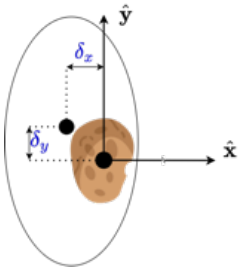

(b) Schematic representation of the physical meaning of δ_x and δ_y

As shown in [30] the set of equations of motion obtained using this new orbit elements $\mathbf{æ} = [A, \alpha, \delta_x, \delta_y, K_5, K_6]$ can be written as:

$$\dot{\mathbf{æ}} = F(\nu, \mathbf{æ}) + G(\nu, \mathbf{æ})\mathbf{u} \tag{14}$$

where the unperturbed dynamics is given by $F(\nu, \mathbf{æ})$:

$$F(\nu, \mathbf{æ}) = \begin{cases} \frac{3}{2}\frac{e\sin(\alpha)}{\gamma^2}\delta_x \\ \frac{3}{2}\frac{e\cos\alpha}{A\gamma^2}\delta_y \\ 0 \\ -\frac{3}{2}\frac{\delta_x}{\gamma^2} \\ 0 \\ 0 \end{cases} \tag{15}$$

while $G(\nu, \mathbf{æ})$ becomes:

$$G(1,1) = -\frac{\gamma \sin(\nu+\alpha) - 2e\sin\alpha}{1-e^2}, \tag{16a}$$

$$G(1,2) = -\frac{e\cos\alpha + (1+\gamma)\cos(\nu+\alpha)}{1-e^2}, \tag{16b}$$

$$G(2,1) = -\frac{\gamma\cos(\nu+\alpha) - 2e\cos\alpha}{A\,(1-e^2)}, \tag{16c}$$

$$G(2,2) = \frac{e\sin\alpha + (1+\gamma)\sin(\nu+\alpha)}{A\,(1-e^2)}, \tag{16d}$$

$$G(3,1) = \frac{2e\gamma\sin(\nu)}{1-e^2}, \tag{16e}$$

$$G(3,2) = \frac{2\gamma^2}{1-e^2}, \tag{16f}$$

$$G(4,1) = \frac{e\gamma\cos(\nu) - 2}{1-e^2}, \tag{16g}$$

$$G(4,2) = -\frac{e(1+\gamma)\sin(\nu)}{1-e^2}, \tag{16h}$$

$$G(5,3) = \cos(\nu), \tag{16i}$$

$$G(6,3) = -\sin(\nu)\ . \tag{16j}$$

The perturbation acceleration $\mathbf{u}$ represents the ellipsoidal gravity field of Phobos and it is computed following the same methodology explained in Section 3.2.1.

3.3 Integral of Motion

The non-autonomous system doesn't allow an integral of motion. However, it is always useful to refer to integral of motions when available, in order to gain a better understanding of the dynamics. For this reason, it is possible to simplify the equations written before by considering Phobos on a circular orbit around Mars. By fixing the eccentricity to zero the equations of motion become autonomous and they allow an integral of motion:

$$J = \frac{1}{2}v - \left[\frac{1}{2}\omega_p(3x^2 - z^2) + U(\mathbf{r})\right] \tag{17}$$

where $\mathbf{r} = [x, y, z]$ is the position vector; v is the norm of the velocity vector; $\mathbf{v} = [\dot{x}, \dot{y}, \dot{z}]$; $U(\mathbf{r})$ is the potential given by the gravity of Phobos [31].
It is possible to rederive the Jacobi constant in function of the orbit elements instead of the state expressed in position and velocity. By substituting $[x, y, z, \dot{x}, \dot{y}, \dot{z}]$ with their equivalent in orbit elements:

$$x = \gamma A\cos(\nu+\alpha) + \delta_x, \tag{18a}$$

$$y = \delta_y - (1+\gamma)A\sin(\nu+\alpha), \tag{18b}$$

$$z = B\sin(\nu+\beta), \tag{18c}$$

$$\dot{x} = -A\sin(\nu+\alpha) - eA\sin(2\nu+\alpha) + \\ - 3eK_4\frac{\sin(\nu)}{\gamma} \tag{18d}$$

$$\dot{y} = -2\gamma A\cos(\nu+\alpha) + eA\cos(\alpha) - 3K_4, \tag{18e}$$

$$\dot{z} = B\cos(\nu+\beta), \tag{18f}$$

the Jacobi constant for the planar case ($z = 0$ and $\dot{z} = 0$) can be computed as follow:

$$J(\mathbf{æ}) = \frac{1}{2}A^2 - \frac{3}{8}\delta_x^2 - U(\mathbf{æ}); \tag{19}$$

where $U(\mathbf{æ})$ is the potential given by the gravity of Phobos expressed in orbit elements.

3.4 Baseline Trajectories

It is not possible to orbit around Phobos in a keplerian-fashion since the mass of the asteroid is too small in relation with the close distance to Mars to outweigh the gravity of Mars. In fact, the Martian moon is so small that its sphere of influence is below its surface and considering the circular restricted three body problem the Lagrange points are very close to its surface [25]. Nonetheless, it is possible to orbit in the vicinity of the Martian Moon by adopting three-body orbits called quasi-satellite orbits (QSO), also known as distant retrograde orbits [32]. These orbits are relative to the orbital plane of Phobos and can be described as 2:1 ellipses centered on the barycenter of the Martian moon. The periodic orbits used as reference (Figure 3) are computed using a differential corrector algorithm [33, 34].
Figure 4-5a-5b show the Jacobi constant and the initial conditions of these orbits in position and velocity and the respective orbit elements.

3.5 Understanding the autonomous system

This section explains the main methodology used to analyze the maps obtained for the autonomous system, where the eccentricity of the orbit of Phobos is set to zero. Even if the main focus of this study is the non-autonomous case, it is important to familiarize with the problem by starting with the autonomous case.
Chaos indicators represent a visual approach to identify the LCSs. This approach is straightforward when the dynamics is two dimensional since the entire phase space can be easily visualized through a 2D plot. However, this is not the case

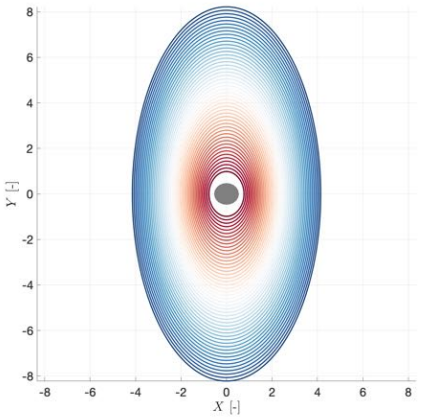

Fig. 3: Family of 2:1 QSOs

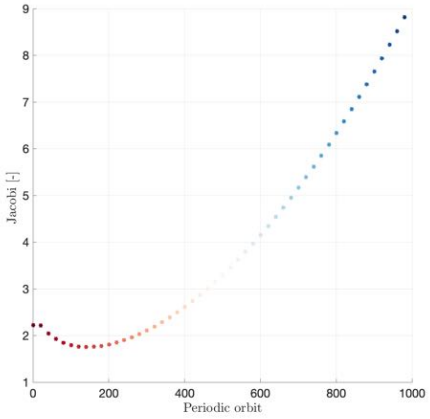

Fig. 4: Jacobi constant of the initial conditions of the different orbits of the 2:1 familys

of many non-linear systems, in particular in astrodynamics, where the state of the spacecraft is usually six dimensional and it is not possible to visualize the entire phase space of the problem but only a two dimensional sub-space. In this case, it is required to include some assumptions and fix some variables in order to lower the dimensionality and reduce the problem to a 2D map [35]. In this section the main strategy for the analysis of the dynamics around Phobos is presented.

It is necessary to choose two variables that define the x-axis and y-axis of the 2D map; 3 variables are then fixed by the user and they remain constant for all the different initial conditions of the grid and fixing the Jacobi constant defines the last variable.

To start creating the maps with a sensible choice of the boundaries of the grid it is helpful to observe how the initial conditions of periodic orbits vary (Figure 5b). If the interest is to identify the bounded motion and the periodic orbits in the proximity of Phobos, the Jacobi constant has to be chosen appropriately and, following the Jacobi constant, the

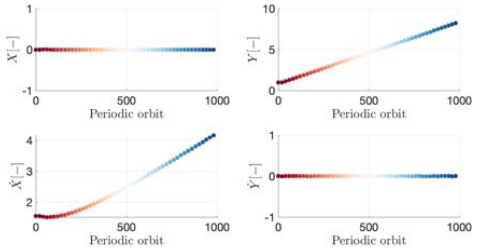

(a) Position and velocity

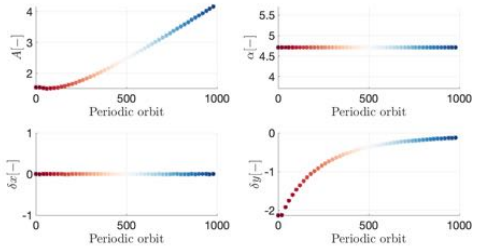

(b) Orbit elements

Fig. 5: Initial conditions of different periodic orbits of the 2:1 family

other orbit elements can be selected. Since the periodic orbits of interests are planar orbits, it is possible to remove the out-of-plane motion by setting K_5 and K_6 to zero, reducing the dimensions of problem to a four. By observing the initial conditions of the periodic orbits, it is clear that the fast changing variable is always $3/2\pi$. By fixing the value of α to $3/2\pi$ only three dimensions are left. The values of A and δ_x are the two values that compose, respectively, the x-axis and y-axis of the 2D map while δ_y can be retrieved by fixing the Jacobi constant.

As shown in section 3.3, the Jacobi constant can be expressed as a function of the orbit elements, but the gravity of Phobos can only be computed numerically. To obtain the value of δ_y a guess is first obtained by considering the spherical gravity field which can be expressed analytically. The Jacobi can be expressed with the spherical gravity of Phobos (J_{sph}) for the normalized case ($\omega_p = 1$ and $\mu_p = 1$):

$$J_{sph}(\mathbf{X}) = \frac{1}{2}(v_x^2 + v_y^2) - \left[\frac{1}{2}(3x^2 - z^2) - \frac{1}{r}\right] \tag{20}$$

while written in orbit elements it becomes:

$$J_{sph}(\mathbf{æ}) = \tfrac{1}{2}A^2 - \tfrac{3}{8}\delta_x^2 - \frac{1}{\sqrt{(A\cos(\theta)+\delta_x)^2+(\delta_y-2A\sin(\theta))^2}} \tag{21}$$

where $\theta = \alpha + \nu$, with $\nu = 0$ and $\alpha = 3/2\pi$.

A first guess for δ_y can be obtained by rederiving Equation 21 in function of δ_y:

$$\begin{aligned} &\delta_y^2 - 4A^*\sin(\theta^*)\delta_y + 4A^{*2}\sin^2(\theta^*) + \\ &+(A^*\cos(\theta^*) + \delta_x^*)^2 - \frac{1}{\left(\frac{1}{2}A^{*2} - \frac{3}{8}\delta_x^{*2} - J^*\right)^2} = 0 \end{aligned} \tag{22}$$

where * represent the fixed parameters.
The guess of δ_y is obtained by solving the quadratic equation in δ_y and taking the smaller between the two possible values. It is interesting to notice that certain combinations of A, δ_x and J might result in imaginary values of δ_y which represent unfeasible initial conditions with the particular choice of the Jacobi and the orbit elements. The δ_y guess is then used as input of a zero-solver method that finds the zero of:

$$\Delta J(\delta_y) = J^* - J(\mathbf{æ}). \tag{23}$$

The value of δ_y found is the one that makes Jacobi constant equal to J^*. This procedure is repeated for all the combinations of A and δ_x that compose the grid while checking that the initial conditions are not inside the surface of Phobos. The initial conditions inside the surface of Phobos are discarded a priori and labeled as crashing conditions.
Once the grid of initial conditions is obtained, the maps are generated following the procedures presented in Chapter 2; note that an event function is included to stop the ingration when the spacecraft passes through Phobos or it escapes from the proximity of Phobos (distance from Phobos larger than 250 km). Table 3 summarizes the parameters used to obtain Figure 7.

Tab. 3: Parameters map in A and δ_x

Symbol	Quantity	Value	Units
e_p	Eccentricity of Phobos	0	-
A_0	Minimum value of A	1.3	-
A_f	Maximum value of A	2.2	-
δ_{x0}	Minimum value of δ_x	-0.5	-
δ_{xf}	Maximum value of δ_x	0.5	-
ν_0	Initial Phase of Phobos	0	-
ν_f	Final Phase of Phobos	$590(30days)$	-
N	Grid size	1000	-
α^*	Fixed value of α	$3/2\pi$	-
J^*	Fixed value of Jacobi constant	2.2	-

To better visualize the bounded regions, the initial conditions that give trajectories that crashed on the Martian Moon or that escaped the system are highlighted in black (-1) and grey (-2) respectively. From the map it is clear that there are two bounded regions for the specific choice of the Jacobi constant. By looking at Figure 4 it is possible to see that there are two periodic orbits for a Jacobi of 2.2. These periodic orbits are highlighted by the green and yellow dots in Figure 7. It is interesting to observe that around the initial conditions of these two periodic orbits two islands of bounded motion are identified. Some sampling of initial conditions have been used (Figure 6) in order to understand the evolution of the different trajectories and, for each state, the nominal trajectory is shown in black while the trajectories in grey correspond the one obtained by the initial conditions with the injection errors (Table 4). As expected, by selecting some initial conditions inside the region of practical stability the motion of the spacecraft stays bounded and the perturbed initial conditions around the chosen state, generated by the Monte Carlo analyses behave in a similar manner (Figure 6a - 6c). When the initial condition is in a very chaotic area, the behaviour of the trajectories around the desired initial condition present clear differences given by the chaoticity of that particular zone of the sub-space, as shown in Figure 6b.

Tab. 4: MMX injection errors

Error	Value	Unit
1σ Position	$[50, 50, 50]$	m
1σ Velocity	$[3, 3, 3]$	cm/s

3.6 Bounded motion in the non-autonomous system

Having understood the autonomous system, it is then interesting to move to the non-autonomous case. To move to the time dependent system it is sufficient to change the eccentricity of Phobos from zero to its actual known value. The same approach for the generation of the map in the autonomous system is here adopted. It is important to highlight that in the non-autonomous system it is not possible to define any integral of motion. Even if the Jacobi is not conserved, it remains interesting to fix an initial value of the Jacobi and use it to define the different initial conditions on the grid as done for the autonomous system.
The parameters used for generating the map shown in Figure 8 are the same presented in Table 3 with the only difference being the value of the eccentricity which was set to $e = 0.0151$ (Table 2).

As for the autonomous case, initial conditions that bring the spacecraft to escape the system or to crash on Phobos are highlighted in grey and black color. It is interesting to observe that the two bounded regions where the two periodic orbits were located are preserved when moving to the non-autonomous system. Figure 9a-9c are two samples taken in the two regions of practical stability. As for the autonomous system, the two sampled initial conditions represent bounded trajectories which are also sufficiently robust to the injection errors envisioned for the MMX mission (Table 4). When an initial condition is selected in a region which is not bounded, like the trajectory 'e', the particular trajectory that is chosen crashes on the Martian moon and the Monte Carlo samples present a chaotic behavior. Similar phenomena appear when selecting initial conditions around the edges between regions of bounded motion, crashing regions and escapes regions.

Having the same maps for the autonomous and non-autonomous case it is possible to over-pose the two, in order to highlight how the different regions change between the two models. In Figure 10a - 10c the points of the grid which iden-

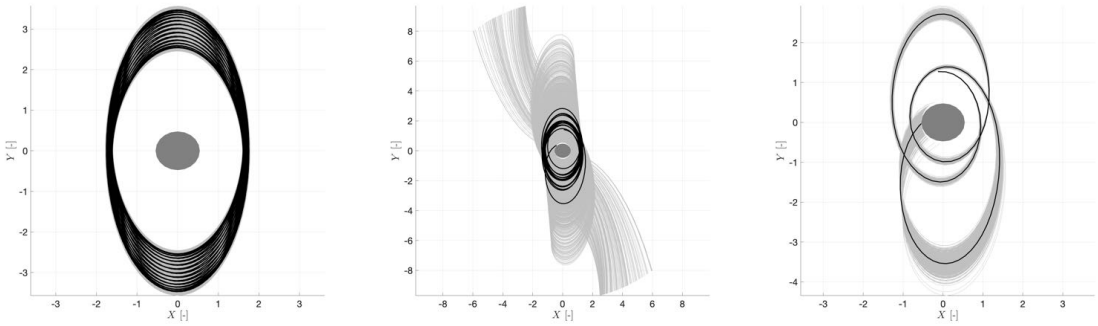

(a) Orbit around Phobos a (b) Orbit around Phobos b (c) Orbit around Phobos c

Fig. 6: Sample orbits in the autonomous system.

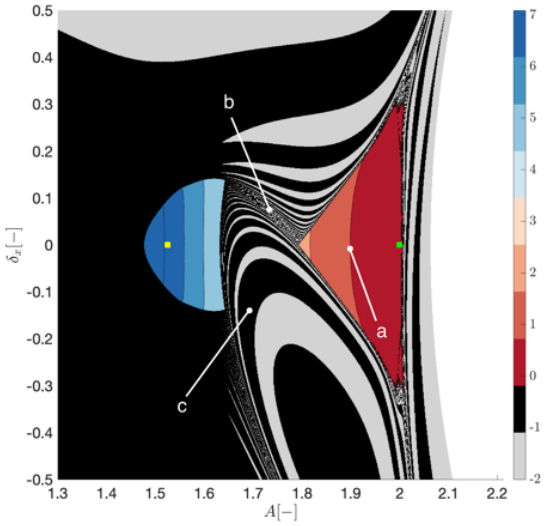

Fig. 7: Map in A and δ_x with $J = 2.2$ in the autonomous system. The yellow and green dot represent the initial conditions of the 2:1 periodic orbits

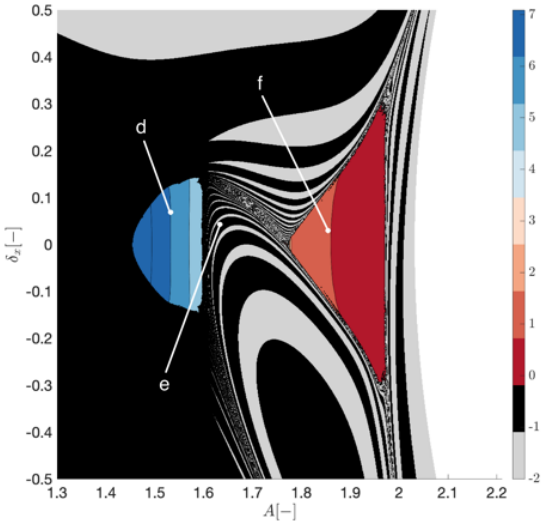

Fig. 8: Map in A and δ_x with $J = 2.2$ for the non-autonomous case.

tify regions of practical stability are highlighted by blue dots for both the autonomous and non-autonomous system. The figure in the middle, Figure 10b, presents the differences between the two maps: in blue are the areas of bounded motion that are present in the autonomous system and are not bounded when the time dependency is added. The red color indicates the zones of bounded regions that are identified in the non-autonomous system and that are not present in the autonomous system. It is interesting to show that when moving from a less representative model to more accurate one, the regions of practical stability don't only decrease but they new areas can appear. As shown in Figure 10 it is possible that the non-autonomous system presents some different regions of bounded motions compared to the autonomous case. By looking at the number of initial conditions that give bounded motion there is a slight decrease in the number of points in the map when moving to the non-autonomous system.

4 Application to the Hera mission

4.1 Dynamics in the vicinity of the Didymos binary system

The perturbed planar bi-elliptic restricted 4-body problem (PBER4BP) describes the motion of a particle in a gravitational field generated by three bodies moving in elliptic orbits. The configuration of the bodies is schematically shown in Figure 11. Let the primaries be Didymos (D1) and Dimorphos (D2). The model is expressed in the synodic reference frame centered at the primaries barycenter, which rotates and pulsates to keep their distance unity [36]. Let $\mu = m_{D2}/(m_{D1} + m_{D2})$, where m_{D1} and m_{D2} are the masses

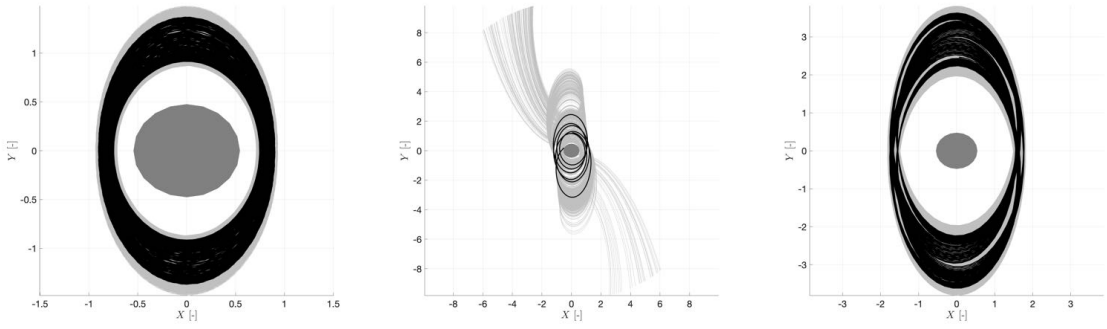

(a) Orbit around Phobos d (b) Orbit around Phobos e (c) Orbit around Phobos f

Fig. 9: Sample orbits in the non-autonomous system.

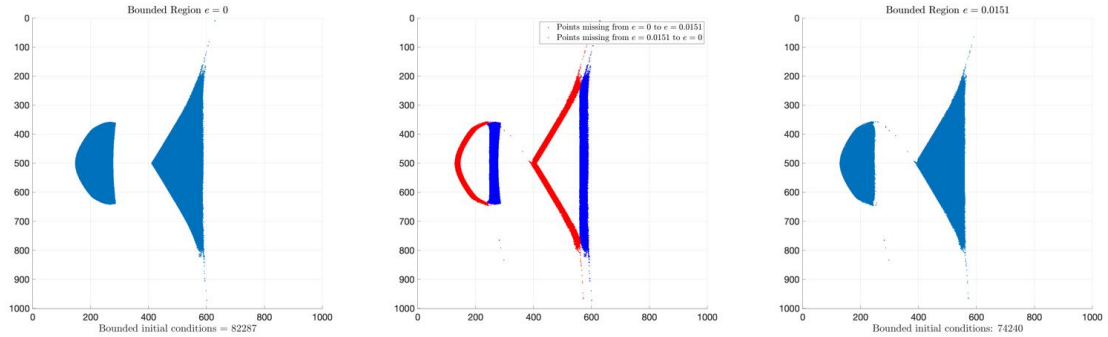

(a) Autonomous system (b) Difference between autonomous and non-autonomous system. (c) Non-autonomous system

Fig. 10: Comparison of practical stability regions between autonomous and non-autonomous system

of D1 and D2, respectively. The positions of D1 and D2 are $(-\mu, 0)$ and $(1-\mu, 0)$, respectively. The equations of motion (EoM) are scaled such that the sum of D1 and D2 masses is set to one as well as their distance, and their period is scaled to 2π [36]. By designating the primaries true anomaly f as the independent variable of the system, the EoM are [36, 37]

$$\mathbf{r}'' + \begin{bmatrix} 0 & -2 \\ 2 & 0 \end{bmatrix} \mathbf{r}' = \nabla\Omega + \\ -\alpha \left(\frac{\mathbf{r}_S}{\|\mathbf{r}_S\|^3} + \frac{\mathbf{r} - \mathbf{r}_S}{\|\mathbf{r} - \mathbf{r}_S\|^3} \right) + \beta \frac{\mathbf{r} - \mathbf{r}_S}{\|\mathbf{r} - \mathbf{r}_S\|^3} \tag{24}$$

$$\theta' = \gamma \frac{(1 + e_S \cos\theta)^2}{(1 - e_S^2)^{3/2}} \frac{(1 - e_D^2)^{3/2}}{(1 + e_D \cos f)^2} \tag{25}$$

where $(\cdot)'$ and $(\cdot)''$ denote the first and second derivatives with respect to the true anomaly f; θ is the true anomaly of the double asteroid barycenter (D) with respect to the Sun (S) and its derivative is obtained through the chain rule [36]; $\mathbf{r} = (x, y)$ and $\mathbf{r}_S = (x_S, y_S)$ are the nondimensional position vectors of the spacecraft and the Sun, respectively, expressed in the synodic reference frame; $\mu_{(\cdot)}$, $a_{(\cdot)}$, and $e_{(\cdot)}$ refer to the gravitational parameter, the semi-major axis, and the eccentricity of the body $(\cdot)$, respectively (see 5). Then, Ω is the potential function that reads [36]

$$\Omega = \frac{1}{1 + e_D \cos f} \left[\frac{1}{2}(x^2 + y^2) + \frac{1 - \mu}{r_{D1}} + \frac{\mu}{r_{D2}} \right] \tag{26}$$

where r_{D1} and r_{D2} are the distances from Didymos and Dimorphos, respectively. The nondimensional coefficients α, β, and γ are computed as

$$\alpha = \frac{\mu_S}{\mu_D (1 + e_D \cos f)}, \tag{27}$$

$$\beta = \frac{P_0 d_{\mathrm{AU}}^2 C_r A}{\mu_D (1 + e_D \cos f) m}, \quad \text{and} \tag{28}$$

$$\gamma = \sqrt{\frac{\mu_S}{\mu_D} \left(\frac{a_D}{a_S} \right)^3} \tag{29}$$

where $P_0 = 4.56\,\mathrm{N\,km^{-2}}$ is the solar radiation pressure (SRP) at 1 AU [38]; $d_{\mathrm{AU}} = 149\,597\,870.700\,\mathrm{km}$ is the Astronomical Unit [38]; $C_r = 1.3$ is the assumed reflectivity coefficient; $A = 0.5\,\mathrm{m}^2$ is the assumed Sun-projected area on the spacecraft for SRP evaluation; $m = 10\,\mathrm{kg}$ is the assumed spacecraft mass.

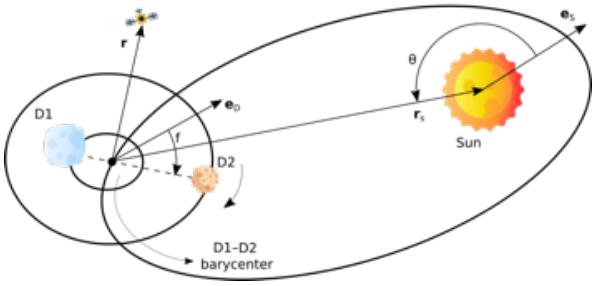

Fig. 11: Schematic representation of the PBER4BP

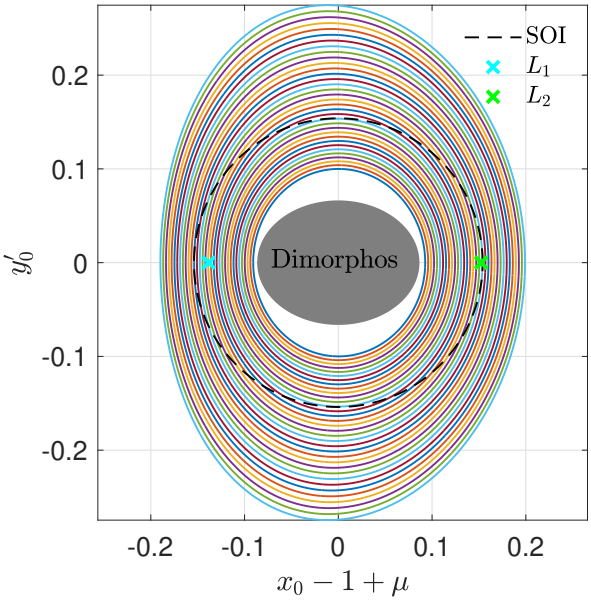

Fig. 12: Family of DROs

The Sun position vector is retrieved according to

$$\mathbf{r}_S = -\frac{(1+e_D\cos f)}{(1+e_S\cos\theta)}\frac{a_S(1-e_S^2)}{a_D(1-e_D^2)} \cdot \begin{bmatrix} \cos f & \sin f \\ -\sin f & \cos f \end{bmatrix} \begin{bmatrix} \cos\theta \\ -\sin\theta \end{bmatrix}. \tag{30}$$

The planar circular restricted 3-body problem (PCR3BP) is recovered setting $\alpha = 0$, $\beta = 0$, and $e_D = 0$ in Eqs. (24), and (26), and by replacing the true anomaly f with the nondimensional time t. The EoM have been integrated with a 8th-order Runge–Kutta integrator with 7th-order error control, the coefficients were derived by Prince and Dormand [39], with relative tolerance set to 10^{-12} [40].

4.2 *Baseline trajectories*

A binary asteroid environment is characterized by a low-gravity field where small dynamical perturbations affect significantly the dynamics [37, 41]. In this work, LDs have been used to get insight on the qualitative behaviour of orbits in the vicinity of the Didymos binary system. Specifically, they have been used to identify regions of bounded motion close to Dimorphos, the tiny moon of Didymos. The LD indicator is computed as presented in Section 2.1. In this study, $f_f = 20\pi$, so corresponding to 10 revolution of the primaries about their common center of mass.

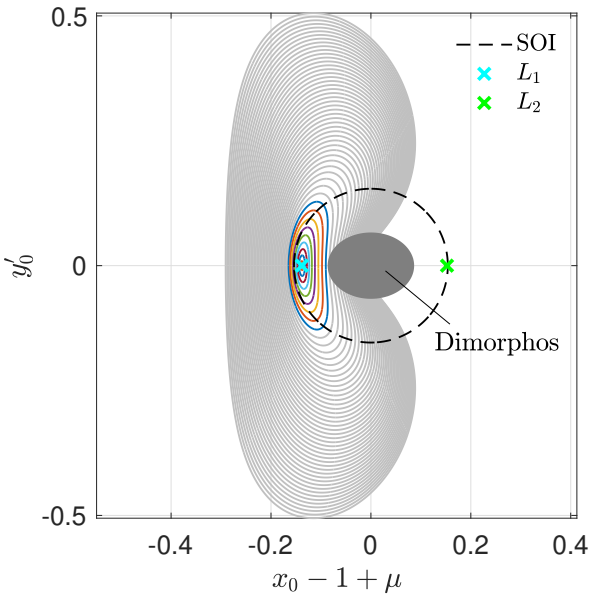

Fig. 13: Family of Lyapunov L_1 orbits

Distant retrograde orbits (DROs) about D2 and Lyapunov orbits (LOs) about the Lagrangian point L_1 have been first computed in the PCR3BP through differential correction [42, 43]. Families of DROs and LOs are shown in Figure 12 and 13. In the specific case of the Didymos system, many LOs impact with the surface of Dimorphos. They are shown in gray in Figure 13.

4.2.1 *Understanding the autonomous system*

The families of periodic orbits are inspected against the LD scalar field of the Didymos system for classification. Our study is focused on the qualitative motion of orbits, thus an initial classification of the region featured by the LD in a simplified autonomous dynamics is necessary. The LD field is computed on the phase space section $y_0 = x_0' = 0$. The same section used to derive through differential correction the initial conditions (ICs) of DROs and LOs families has been used. The grid of ICs is defined on the domain $x_0 \in [-0.35, -0.05]$ and $y_0' \in [0.3, 0.9]$, with grid resolution 400×400. The map presented in Figure 14 shows the results of the classification procedure. Levels -2 and -1 corresponds to escape and crash trajectories, respectively. A trajectory is considered to escape from D2 when the particle distance from the center of the moon is larger then a_D. The portion of the LOs family plotted in the map completely crash against D2. Conversely, the DROs family is fully contained within two basins of ICs separated by a bottleneck. The basin located further from D2 develops in a

Tab. 5: Physical properties Didymos system.

Symbol	Quantity	Value	Units
μ	Mass ratio parameter	$9.214\,228 \times 10^{-3}$	-
μ_D	Didymos system gravitational parameter	$3.522\,601 \times 10^{-8}$	$\mathrm{km}^3\,\mathrm{s}^{-2}$
μ_S	Sun gravitational parameter	$1.327\,124 \times 10^{11}$	$\mathrm{km}^3\,\mathrm{s}^{-2}$
a_D	Dydimos system semi-major axis	1.19	km
a_S	Sun–Didymos system semi-major axis	$2.460\,287 \times 10^{8}$	km
e_D	Dydimos system eccentricity	0.03	-
e_S	Sun–Didymos system eccentricity	0.383 638	-
R_{D1}	Didymos radius	390	m
$R_{x,D2}$	Dimorphos semi-major axis	103	m
$R_{y,D2}$	Dimorphos semi-minor axis	79	m

long narrow channel containing several bounded orbits resembling large DROs in shape.

Three baseline trajectories (orbits 'a', 'b', and 'c' in Figure 15) have been selected by visual inspection. They are shown with dots in Figure 14, while their exact ICs are reported in Table 6. Orbit 'a' exhibits bounded motion, it is located in the basin closest to Dimorphos, and it is very similar to a small DRO (see Figure 15a). Orbit 'b' still exhibits bounded motion but it is located very far from D2, in a region where the differential correction scheme failed in finding periodic orbits (see Figure 15b). The last baseline trajectory, orbit 'c', crashes on Dimorphos surface and it is a quasi-LO (see Figure 15c).

The robustness of the selected baseline trajectories have been assessed through a Monte Carlo simulation, where 1000 trajectories with perturbed initial states have been propagated. The perturbed initial states have been derived assuming injection errors on position $\Delta r_0 = 0.5\,\mathrm{m}$ and on velocity $\Delta v_0 = 0.5\,\mathrm{mm\,s}^{-1}$. Those are at least 2 order of magnitudes smaller than the expected injection errors for the Hera's CubeSats [44, 45], but such precision seems required to fly DROs about D2 when only the point mass gravitational contributions of the primaries are considered.

The results of the robustness analysis are shown in Figure 15, where perturbed trajectories are plotted in gray. As can be seen in Figure 15b, orbit 'b' appears less robust than orbits 'a' and 'c'. In fact, not all perturbed initial states retain the qualitative behavior of the baseline trajectory.

4.2.2 *Bounded motion in the non-autonomous system*

The identification of bounded motion regions in a more representative, non-autonomous dynamical model follows. The LD scalar field computed in the perturbed PBER4BP is shown in Figure 16. The field has been computed when the Didymos binary system is at the aphelion. Specifically, in the propagations $\theta_0 = \pi$ at true anomaly f_0. For comparison, the map reports the families of periodic orbits and the location of the Lagrange point L_1 computed in the PCR3BP. The major features of the map are retained also in the PBER4BP. However, accounting for the presence of the Sun gravitational attraction

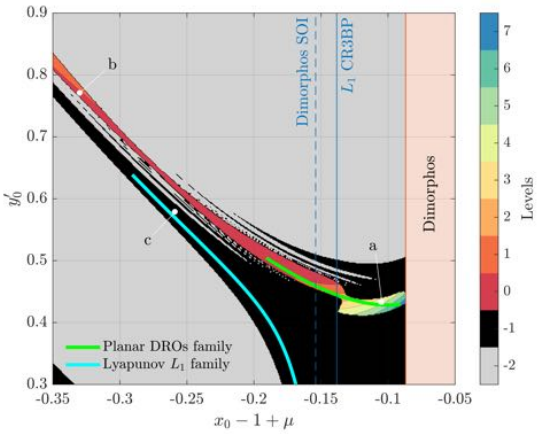

Fig. 14: LD scalar field computed in the PCR3BP

and the SRP changed completely the qualitative behavior of the nearest to D2 bounded motion basin visible in Figure 14. Differently, the other region of bounded motion is maintained although narrowed. Some visible changes in the map were expected since these perturbations, particularly the SRP, have a strong effect on the dynamics when flying in low-gravity environment [37, 41].

Also in this case, three baseline trajectories (orbits 'd', 'e', and 'f' in Figure 17) have been selected. They are indicated as white dots in Figure 16. Orbit 'd' is located in the only region of bounded motion that still exists in the map. It is located relatively close to the DROs family computed in the PCR3BP, as a consequence its shape resembles a DRO (see Figure 17a). Orbit 'e' is a trajectory impacting on Didymos surface and it is shown in Figure 17b. Finally, orbit 'f' has been chosen from a chaotic region where different kind of behaviors are concentrated in a small portion of the phase space (see Figure 17c).

In a similar fashion as before, a robustness analysis on the selected baseline trajectories have been carried out via a Monte Carlo simulation. In this case, except for orbit 'e', the baseline trajectories resulted to be less robust to perturbations. In particular, many perturbed initial states diverge from orbit 'd'. Regarding orbit 'f', it belonging to a chaotic region, it is not surprising that the trajectory resulted not robust at all.

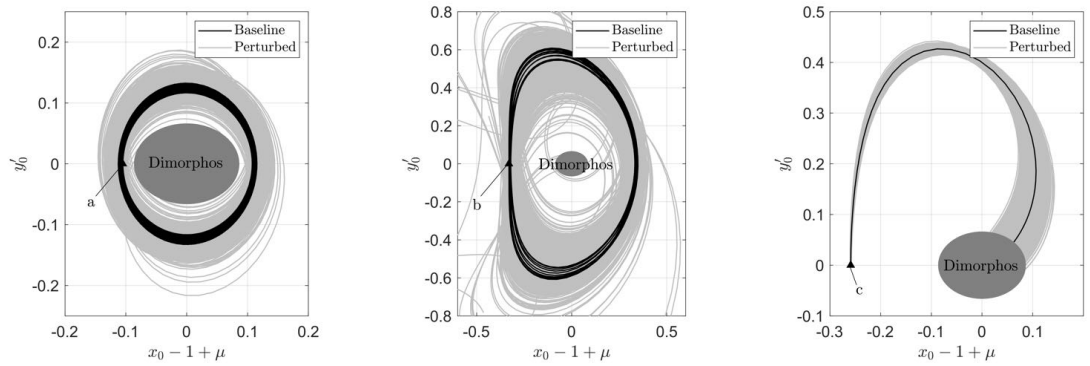

(a) Orbit around Dimorphos a (b) Orbit around Dimorphos b (c) Orbit around Dimorphos c

Fig. 15: Sample orbits in the PCR3BP.

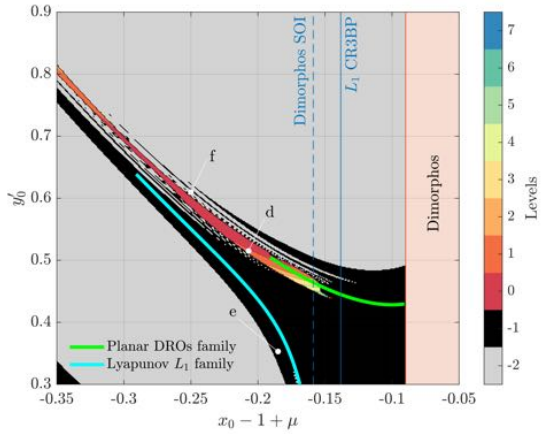

Fig. 16: LD scalar field computed in the perturbed PBER4BP

Tab. 6: ICs baseline trajectories for Hera mission.

Orbit	**Initial condition**				
	$x_0 - 1 - \mu$	y_0	x_0'	y_0'	θ_0
a	-0.105	0	0	0.433	-
b	-0.330	0	0	0.771	-
c	-0.259	0	0	0.579	-
d	-0.207	0	0	0.515	π
e	-0.185	0	0	0.353	π
f	-0.250	0	0	0.610	π

5 Conclusion

In this paper Lagrangian Descriptors were adopted as chaos indicators in order to detect coherent patterns in time-dependent dynamical system to identify practical stability regions to be exploited for the design of bounded orbits around small bodies.

For the MMX mission it was possible to clearly detect the bounded motion around 2:1 QSOs by selecting a grid of initial conditions fixing the Jacobi constant. The approach with the Jacobi constant enabled to detect similar regions of practical stability in the non-autonomous system. The trajectories selected in the bounded regions for both autonomous and non-autonomous systems were shown to be robust to injections errors.

For the Hera mission it was shown that fixing four out of the six dimensions and building the grid of initial conditions by changing only two parameters enabled to detect the entire families of periodic orbit on the maps. Due to the strong effect given by the solar radiation pressure a more significant difference was detected between the two models compared to the MMX case. The Monte Carlo analysis showed that not all the practical stability regions might be robust to the particular injection errors that were selected and it suggests that, if similar orbits had to be chosen, stronger requirements on the injection errors should be required.

Future research will focus in exploring different combinations of variables in order to highlight other families periodic orbits and expand the current results, including the out-of-plane motion.

Acknowledgments

This work has received funding from the French space agency, Centre National d'Études Spatiales (CNES), under the Research and Technology (R&T) programme, contract R-S20/BS-0005-066.

Bibliography

[1] DS Lauretta, SS Balram-Knutson, E Beshore, WV Boynton, C Drouet d'Aubigny, DN DellaGiustina, HL Enos, DR Golish, CW Hergenrother, ES Howell, et al. Osiris-rex: sample return from asteroid (101955) bennu. *Space Science Reviews*, 212(1):925–984, 2017.

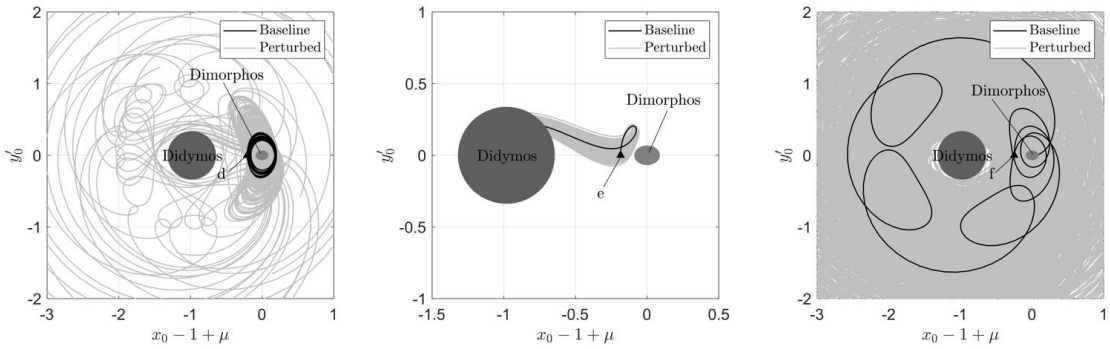

(a) Orbit around Dimorphos d (b) Orbit around Dimorphos e (c) Orbit around Dimorphos f

Fig. 17: Sample orbits in the perturbed PBER4BP

[2] Andreas M Hein, Michael Saidani, and Hortense Tollu. Exploring potential environmental benefits of asteroid mining. *arXiv preprint arXiv:1810.04749*, 2018.

[3] Andy F Cheng, J Atchison, Brian Kantsiper, Andrew S Rivkin, A Stickle, Cheryl Reed, Andres Galvez, Ian Carnelli, Patrick Michel, and S Ulamec. Asteroid impact and deflection assessment mission. *Acta Astronautica*, 115:262–269, 2015.

[4] George Haller. A variational theory of hyperbolic lagrangian coherent structures. *Physica D: Nonlinear Phenomena*, 240(7):574–598, 2011.

[5] Francois Lekien, Shawn C Shadden, and Jerrold E Marsden. Lagrangian coherent structures in n-dimensional systems. *Journal of Mathematical Physics*, 48(6):065404, 2007.

[6] Douglas H Kelley, Michael R Allshouse, and Nicholas T Ouellette. Lagrangian coherent structures separate dynamically distinct regions in fluid flows. *Physical Review E*, 88(1):013017, 2013.

[7] Alireza Hadjighasem, Mohammad Farazmand, Daniel Blazevski, Gary Froyland, and George Haller. A critical comparison of lagrangian methods for coherent structure detection. *Chaos: An Interdisciplinary Journal of Nonlinear Science*, 27(5):053104, 2017.

[8] Mohammad Farazmand and George Haller. Computing lagrangian coherent structures from their variational theory. *Chaos: An Interdisciplinary Journal of Nonlinear Science*, 22(1):013128, 2012.

[9] Daniel Blazevski and George Haller. Hyperbolic and elliptic transport barriers in three-dimensional unsteady flows. *Physica D: Nonlinear Phenomena*, 273:46–62, 2014.

[10] Jack Tyler and Alexander Wittig. An improved numerical method for three-dimensional hyperbolic lagrangian coherent structures using differential algebra. *arXiv preprint arXiv:2204.06236*, 2022.

[11] David J Gondelach, Roberto Armellin, and Alexander Wittig. On the predictability and robustness of galileo disposal orbits. *Celestial Mechanics and Dynamical Astronomy*, 131(12):1–30, 2019.

[12] Daniel Pérez-Palau, Josep J Masdemont, and Gerard Gómez. Tools to detect structures in dynamical systems using jet transport. *Celestial mechanics and dynamical astronomy*, 123(3):239–262, 2015.

[13] Evan S Gawlik, Jerrold E Marsden, Philip C Du Toit, and Stefano Campagnola. Lagrangian coherent structures in the planar elliptic restricted three-body problem. *Celestial mechanics and dynamical astronomy*, 103(3):227–249, 2009.

[14] Massimiliano Guzzo and Elena Lega. Geometric chaos indicators and computations of the spherical hypertube manifolds of the spatial circular restricted three-body problem. *Physica D: Nonlinear Phenomena*, 373:38–58, 2018.

[15] M Manzi and F Topputo. A flow-informed strategy for ballistic capture orbit generation. *Celestial Mechanics and Dynamical Astronomy*, 133(11):1–16, 2021.

[16] Aalok Parkash. Application of lagrangian coherent structures to the computation and understanding of ballistic capture trajectories. 2019.

[17] N Baresi and Y Kawakatsu. Quasi-periodic motion around phobos: applications to the martian moons exploration (mmx). In *32nd International Symposium on Space Technology and Science, Fukui, Japan*, 2019.

[18] Tomoki Nakamura, Hitoshi Ikeda, Toru Kouyama, Hiromu Nakagawa, Hiroki Kusano, Hiroki Senshu, Shingo Kameda, Koji Matsumoto, Ferran Gonzalez-Franquesa, Naoya Ozaki, et al. Science operation plan of phobos and deimos from the mmx spacecraft. *Earth, Planets and Space*, 73(1):1–27, 2021.

[19] S C Shadden, F Lekien, and J E Marsden. Definition and properties of lagrangian coherent structures from finite-time lyapunov exponents in two-dimensional aperiodic flows. *Physica D: Nonlinear Phenomena*, 212(3-4):271–304, 2005.

[20] C R Short, D Blazevski, K C Howell, and G Haller. Stretching in phase space and applications in general nonautonomous multi-body problems. *Celestial Mechanics and Dynamical Astronomy*, 122(3):213–238, 2015.

[21] Carlos Lopesino, Francisco Balibrea-Iniesta, Víctor J García-Garrido, Stephen Wiggins, and Ana M Mancho. A theoretical framework for lagrangian descriptors. *International Journal of Bifurcation and Chaos*, 27(01):1730001, 2017.

[22] Ana M. Mancho, Stephen Wiggins, Jezabel Curbelo, and Carolina Mendoza. Lagrangian descriptors: A method for revealing phase space structures of general time dependent dynamical systems. *Communications in Nonlinear Science and Numerical Simulation*, 18(12):3530–3557, 2013.

[23] C Mendoza, A Mancho, and S Wiggins. Lagrangian descriptors and the assessment of the predictive capacity of oceanic data sets. *Nonlinear Processes in Geophysics*, 21:677–689, 06 2014.

[24] Vıctor J Garcıa-Garrido. A tutorial on the method of lagrangian descriptors. 2019.

[25] Nicola Baresi, Diogene A Dei Tos, Hitoshi Ikeda, and Yasuhiro Kawakatsu. Trajectory design and maintenance of the martian moons exploration mission around phobos. *Journal of Guidance, Control, and Dynamics*, pages 1–12, 2020.

[26] D.J. Scheeres, S. Van wal, Z. Olikara, and N. Baresi. Dynamics in the phobos environment. *Advances in Space Research*, 63(1):476–495, 2019.

[27] BC Carlson. Computing elliptic integrals by duplication. *Numerische Mathematik*, 33(1):1–16, 1979.

[28] Koji Yamanaka and Finn Ankersen. New state transition matrix for relative motion on an arbitrary elliptical orbit. *Journal of guidance, control, and dynamics*, 25(1):60–66, 2002.

[29] F Cabral and P Gil. *On the stability of Quasi-Satellite orbits in the elliptic restricted three-body problem*. PhD thesis, Master's thesis, Universidade Técnica de Lisboa, 2011.

[30] Nicola Baresi, Lamberto Dell'Elce, Josué Cardoso dos Santos, and Yasuhiro Kawakatsu. Long-term evolution of mid-altitude quasi-satellite orbits. *Nonlinear Dynamics*, 99(4):2743–2763, 2020.

[31] DJ Scheeres, Z Olikara, N Baresi, et al. Dynamics in the phobos environment. *Advances in Space Research*, 63(1):476–495, 2019.

[32] Elisabet Canalias, Laurence Lorda, and Julien Laurent-Varin. Design of realistic trajectories for the exploration of phobos. In *2018 Space Flight Mechanics Meeting*, page 0716, 2018.

[33] M Lara and J Peláez. On the numerical continuation of periodic orbits-an intrinsic, 3-dimensional, differential, predictor-corrector algorithm. *Astronomy & Astrophysics*, 389(2):692–701, 2002.

[34] Nicola Baresi, Xiaoyu Fu, and Roberto Armellin. A high-order taylor polynomials approach for continuing trajectories in restricted three-body problems. In *2020 AAS/AIAA Astrodynamics Specialist Conference*, 2020.

[35] Jared M Maruskin. *Introduction to dynamical systems and geometric mechanics*. Solar Crest Publishing LLC, 2012.

[36] N Hyeraci and F Topputo. Method to design ballistic capture in the elliptic restricted three-body problem. *Journal of Guidance, Control, and Dynamics*, 33(6):1814–1823, 2010. DOI: 10.2514/1.49263.

[37] F Ferrari, V Franzese, M Pugliatti, C Giordano, and F Topputo. Trajectory options for Hera's Milani CubeSat around (65803) Didymos. *The Journal of the Astronautical Sciences*, 68(4):973–994, 2021. DOI: 10.1007/s40295-021-00282-z.

[38] H Curtis. *Orbital Mechanics for Engineering Students: Revised Reprint*. Butterworth-Heinemann, 2020. DOI: 10.1016/C2020-0-01873-6.

[39] P Prince and J Dormand. High order embedded Runge-Kutta formulae. *Journal of computational and applied mathematics*, 7(1):67–75, 1981. DOI: 10.1016/0771-050x(81)90010-3.

[40] Z-F Luo, F Topputo, F Bernelli-Zazzera, and G Tang. Constructing ballistic capture orbits in the real Solar System model. *Celestial Mechanics and Dynamical Astronomy*, 120(4):433–450, 2014. DOI: 10.1007/s10569-014-9580-5.

[41] F Ferrari, V Franzese, M Pugliatti, C Giordano, and F Topputo. Preliminary mission profile of Hera's Milani CubeSat. *Advances in Space Research*, 67(6):2010–2029, 2021. DOI: 10.1016/j.asr.2020.12.034.

[42] K C Howell. Three-dimensional, periodic, 'halo' orbits. *Celestial Mechanics*, 32(1):53–71, 1984. DOI: 10.1007/bf01358403.

[43] R Russell. Global search for planar and three-dimensional periodic orbits near Europa. *The Journal of the Astronautical Sciences*, 54(2):199–226, 2012. DOI: 10.1007/BF03256483.

[44] C Bottiglieri, F Piccolo, A Rizza, C Giordano, M Pugliatti, V Franzese, F Ferrari, and F Topputo. Trajectory design and orbit determination of hera's milani cubesat. In *2021 AAS/AIAA Astrodynamics Specialist Conference*, pages 1–15, 2021.

[45] C Bottiglieri, F Piccolo, A Rizza, M Pugliatti, V Franzese, C Giordano, F Ferrari, and F Topputo. Mission analysis and navigation assessment for hera's milani cubesat. In *4S Symposium*, pages 1–12, 2022.